UCLA
UCLA Previously Published Works

Title
Finger-powered electrophoretic transport of discrete droplets for portable digital microfluidics.

Permalink
https://escholarship.org/uc/item/45w910s2

Journal
Lab on a chip, 16(13)

ISSN
1473-0197

Authors

Peng, Cheng
Wang, Yide
Sungtaek Ju, Y

Publication Date
2016-07-01

DOI
10.1039/c6lc00219f

Peer reviewed

Finger-powered electrophoretic transport of discrete droplets for portable digital microfluidics†

Cheng Peng, Yide Wang and Y. Sungtaek Ju*

We report a finger-powered digital microfluidic device based on the electrophoretic transport of discrete droplets (EPD). An array of piezoelectric elements is connected in parallel to metal electrodes immersed in dielectric fluids. When deflected in a controlled sequence *via* human finger power, the piezoelectric elements charge and actuate droplets across each electrode pair through electrophoretic force. Successful droplet transportation requires the piezoelectric elements to provide both sufficient charge and voltage pulse duration. We quantify these requirements using numerical models to predict the electrical charges induced on the droplets and the corresponding electrophoretic forces. The models are experimentally validated by comparing the predicted and measured droplet translational velocities. We successfully demonstrated transport and merging of aqueous droplets over a range of droplet radii (0.6–0.9 mm). We further showed direct manipulation of body fluids, including droplets of saliva and urine, using our finger-powered EPD device. To facilitate practical implementation of multistep assays based on the approach, a hand/finger-rotated drum system with a programmable pattern of protrusions is designed to induce deflections of multiple piezoelectric elements and demonstrate programmable fluidic functions. An electrode-to-piezoelectric element connection scheme to minimize the number of piezoelectric elements necessary for a sequence of microfluidic functions is also explored. The present work establishes an engineering foundation to enable design and implementation of finger-powered portable EPD microfluidic devices.

Introduction

Microfluidic devices that do not require bulky peripheral hardware, such as pumps and external batteries/power supplies, are highly desirable for portable applications outside the traditional laboratory context, such as point-of-care (POC) and other portable diagnostics, bio-surveillance, forensics, and environmental sampling. One option is paper-based microfluidic devices, which have emerged as a simple and low-cost microfluidic paradigm that eliminates the need for external pumps.[1–7] Recent studies further proposed schemes to improve the fluid handling accuracy of paper-based microfluidic devices.[8,9] Other "passive" pumping mechanisms for microfluidic devices include "degas driven flows",[10,11] capillary pumps,[12,13] finger-powered hydrodynamic flows[14] and punch-card based programmable microfluidic devices.[15] However, most of these schemes involve pre-defined microfluidic channel structures, which limit their functional flexibility and make them difficult to scale up.

Digital microfluidic devices are attractive because they deal with discrete droplets individually and therefore can pro-

vide more on-demand flexibility and versatility. One prominent example is devices based on the electrowetting on dielectric (EWOD) phenomenon. Recent studies reported advances in digital microfluidic devices[16] to facilitate device fabrication and reduce operating voltages, but they still required external electric power sources. We recently reported one implementation of finger-powered EWOD devices.[17] Droplet pinning and contamination due to surface adsorption, however, present practical technical challenges.

Electrophoretic control of discrete droplets (EPD) is a promising alternative approach for digital microfluidics. EPD utilizes rapid charging of conductive droplets by adjacent electrodes and their subsequent electrophoretically induced motion.[18,19] Both the droplet and the electrodes are typically immersed in a dielectric fluid. This is advantageous because EPD minimizes direct liquid–solid contact when compared with other droplet actuation methods such as EWOD, thermomechanical[20] and surface acoustic wave (SAW)-driven[21] actuations.

Previous studies[22–24] of EPD investigated the electrophoretic force and resulting trajectories of a droplet suspended between parallel plates or other macroscale electrodes. EPD is typically thought to require very high voltages,[25] ill-suited for portable applications. However, actuation voltages can be reduced well below 500 V through miniaturization.

Mechanical and Aerospace Engineering, University of California, Los Angeles, USA.
E-mail: sungtaek.ju@ucla.edu
† Electronic supplementary information (ESI) available. See DOI: 10.1039/c6lc00219f

In the present work, we report a finger-powered EPD digital microfluidic device. An array of piezoelectric elements is connected in parallel to electrodes immersed in dielectric fluids, as shown in Fig. 1. When deflected by human fingers, the piezoelectric elements establish an electric field across adjacent EP electrodes to charge and actuate a droplet through electrophoretic force. We report numerical models and their experimental validation to help develop design/selection criteria for successful droplet charging and actuation. We experimentally demonstrated the transport and merging of aqueous droplets of a range of radii (~0.6 to 0.9 mm). Further, we performed direct manipulation of droplets of various body fluids using our finger-powered EPD to facilitate the exploration of its potential biomedical applications. Next, to facilitate practical system-level implementation of our concept, we design and develop a mechanical system to translate human-finger (or hand) power into a sequence of precisely controlled and reproducible deflections of multiple piezoelectric elements. In addition, given the limited number of piezoelectric elements one can incorporate in practical portable devices, electrode matrix designs and electric connection schemes have also been explored to realize different microfluidic functions while minimizing the number of piezoelectric elements required. We experimentally demonstrated the pre-programmed functional actuation of droplets on a 4 × 4 base electrode matrix using our integrated mechanical system.

Modelling of induced droplet charge and electrophoretic force

For successful transport of a droplet across adjacent EP electrodes, the piezoelectric elements need to provide sufficient charges and electric bias to generate appropriate electrophoretic forces. We first develop finite element models to predict the induced droplet charges and resulting electrophoretic force for a range of droplet sizes, electrode pitches, and actuation voltages anticipated in typical microfluidic applications.

Fig. 2 illustrates our simulation domain. Two cylindrical electrodes of radius r_c and pitch p and a spherical droplet of radius r are immersed in a dielectric fluid (Fluid 1). A second
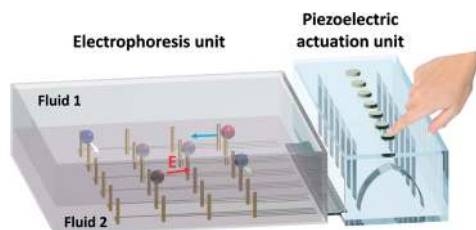

Fig. 1 Schematic illustration of one implementation of our finger-powered EPD device. An electric field is established across adjacent EP electrodes when the corresponding piezoelectric elements are deflected by human fingers (or finger-powered mechanical levers).
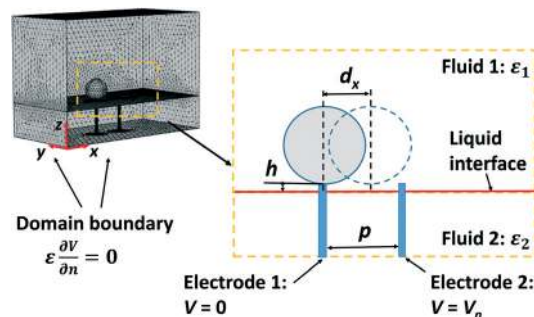

Fig. 2 A finite element model used to predict the electric charges acquired by a droplet suspended between two biased electrodes and the resulting electrophoretic force.

fluid of a higher density (Fluid 2) is used to separate the droplet from the solid surface at the bottom. The electrodes protrude into Fluid 1 by a finite gap of h. The dielectric constants of the two fluids are denoted as ε_1 and ε_2, respectively. A DC voltage of magnitude V_p is applied to Electrode 2, while Electrode 1 is grounded.

The droplet is initially in contact with the upper surface of Electrode 1. The droplet quickly reaches an equipotential state with the electrode, with electric charges of the same polarity distributed over the droplet surface. We assume that the droplet takes the maximum equilibrium charges before it leaves the charging electrode. A further discussion of this assumption is provided in Appendix A. The charged droplet then detaches from the electrode under repulsive electrophoretic force acting on the acquired charges. The parameter d_x is defined as the location of the droplet center from its charging electrode (Electrode 1) along the x axis.

The electric field $E = -\nabla V$ is obtained by solving the Laplace equation in both upper and lower dielectric fluids:

$$\nabla^2 V = 0 \tag{1}$$

The free charge density is set to be 0 in the dielectric fluids.

The droplet is initially in contact with Electrode 1, and we specify the following boundary conditions:

$$V = 0 \quad \text{on Electrode 1} \tag{2}$$

$$V = V_n \quad \text{on Electrode 2} \tag{3}$$

$$V_d = 0 \quad \text{on the droplet surface} \tag{4}$$

At the outer boundaries, we specify the zero charge or symmetry boundary conditions:

$$\varepsilon \frac{\partial V}{\partial n} = 0 \tag{5}$$

Once the electric field E is obtained, we calculate the droplet total charge Q_{eq} by integrating the electric displacement over the droplet surface S_d:

$$Q_{cq} = \varepsilon \int \vec{E} dS \qquad (6)$$

The lateral electrophoretic force F_e along the x axis is calculated by integrating the Maxwell stress tensor over S_d:

$$F_e = \frac{\varepsilon}{2} \int E_n^2 \cos\theta dS \qquad (7)$$

Here, E_n is the electric field normal to the droplet surface and θ is the angle between the surface normal vector and the x axis.

We next determine the electrophoretic force acting on the droplet at different positions between the two adjacent electrodes assuming that the total droplet surface charge is equal to that obtained in eqn (6): $Q = Q_{eq}$. As the droplet moves, the electric field distribution is modified (E'). We solve the Laplace equation for each droplet location to determine E' and then calculate the electrophoretic force using eqn (7) under this new electric field distribution.

Experimental setup

We use a device schematically illustrated in Fig. 1 to study finger-powered EPD operations. A transparent acrylic cell is filled with two immiscible dielectric liquids. The two liquids are chosen to have densities and surface tensions such that spherical aqueous droplets stay near the interface of the two liquids. In the present study, we selected silicone oil (DC 200F, v = 5 cSt, σ = 10^{-13} S m^{-1}, ε = $2.8\varepsilon_0$) and Fluorinert FC-40 (ε = $1.9\varepsilon_0$). Insulated copper electrodes of diameter ~0.18 mm are assembled to form an array with pitch p. The top surfaces of the electrodes are exposed to allow for droplet charging. Aqueous droplets are placed into the cell using a micropipette (Eppendorf, 0.1–2.5 µL). Different kinds of aqueous droplets are tested, including those of DI water (ρ = 0.1–1 MΩ), human body fluids (saliva and urine), and a sodium hydroxide solution, covering pH values from 5.6 to 9.

The actuation unit consists of laminated polymeric piezoelectric elements (Measurement Specialist, LDT Series) with active layers (polyvinylidene fluoride) of thickness 28 µm and size 1.3 × 2.5 cm^2. A pair of piezoelectric elements are connected in series to increase the voltage output. The negative terminal of each piezoelectric unit is grounded, while the positive terminal is connected to each individual EP electrode (see Fig. S1 in the ESI†). With this arrangement, when adjacent units are deflected in opposite directions, a voltage differential of approximately 200 V can be generated across two EP electrodes.[17] This output is then used to charge a droplet and establish an electric field necessary for droplet actuation.

Results and discussion

Droplet charges

Fig. 3 shows the predicted equilibrium charges Q_{eq} for various combinations of droplet sizes and electrode pitches un-
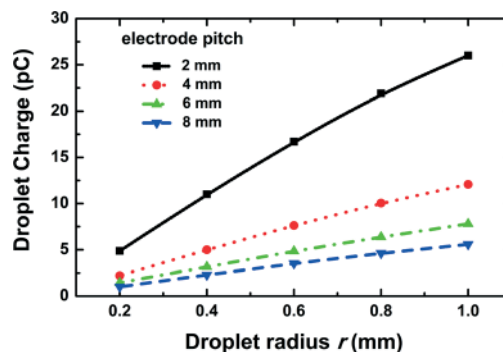

Fig. 3 Predicted droplet equilibrium charge Q_{eq} as a function of the droplet size under an electrode bias voltage V_p of 200 V. The results are shown for different electrode pitches, varying from 2 to 8 mm.

der an actuation voltage of 200 V. The droplet radius r was varied from 0.2 to 1 mm and the electrode pitch p from 2 to 8 mm. The actuation voltage is chosen to be comparable to outputs from commercial piezoelectric elements we used in the present study.

The predicted charges are in the range of a few to a few tens of pC. These translate into equivalent capacitances of approximately 10^{-2} to 10^{-1} pF (given an applied voltage of 200 V) for our droplet/electrode system. To provide sufficient charges to the droplet while maintaining the electric bias field during droplet transportation, the capacitance of the piezoelectric elements must be much larger than this value. This represents one criterion, in terms of the minimum capacitance, in designing piezoelectric elements.

The capacitance of our piezoelectric elements is approximately 1.3 nF, more than 4 orders of magnitude greater than the equivalent capacitances of the droplet/electrodes. The amount of charges generated by our piezoelectric elements at an output voltage of 200 V (approximately 2.6×10^{-7} C) is likewise more than 4 orders of magnitude larger than the amount of charges acquired by the droplet. As a result, the flow of charges from the piezoelectric elements to the droplet would have minimal impact on the electrode bias voltages. The actuation voltages may therefore be approximated as a constant equal to the open circuit output voltage of the piezoelectric elements.

For reference, Table 1 lists the estimated capacitances per unit area of two common types of piezoelectric elements with two different thicknesses.[26,27]

Fig. 3 also reveals that, for a given droplet size, the total amount of charges decreases with increasing electrode

Table 1 Capacitances of typical piezoelectric elements per unit area

Material	Relative permittivity	Film thickness (µm)	Capacitance per unit area (pF mm^{-2})
PVDF	12.4	25	4.4
PVDF	12.4	100	1.1
PZT-5A	1600	25	531
PZT-5A	1600	100	132

pitches or decreasing nominal electric fields E_{nom} under a constant bias voltage. The nominal electric field is defined as $E_{nom} = V_p/p$. This is expected since the equilibrium droplet charges depend on the electric displacement on the droplet surface, which is in turn proportional to the electric field strength.

We also note that the droplet surface charge density decreases rapidly with increasing droplet sizes, resulting in a nearly linear increase in the total droplet charges with the droplet radius. This is in part because droplet charging is governed primarily by highly non-uniform electric fields in the immediate vicinity of the electrode tip, whose magnitudes decrease rapidly with distance from the electrode tip.

To illustrate these points further, we consider a case of a droplet of radius r suspended between two large parallel plate electrodes. The amount of equilibrium charges under this configuration ($Q_{parallel}$) is given as follows:

$$Q_{parallel} = \frac{\pi}{6}\left(4\pi r^2\right)\varepsilon E. \qquad (8)$$

The predicted droplet charges are plotted for various combinations of droplet sizes and electrode pitches in Fig. 4 for $E_{nom} = 0.01$ MV m^{-1}, 0.1 MV m^{-1} and 1 MV m^{-1}. The normalized charges are approximately inversely proportional to the normalized droplet radius for electrode and droplet geometric parameters considered in the present study. This is consistent with the nearly linear relation between the amount of droplet charges and the droplet radius observed in Fig. 3.

Droplet velocity and electrophoretic force

To establish baselines, we first conducted experiments where we actuate droplets using an external power supply. The droplet translational motions are recorded using a digital camera at 30 fps. The instantaneous droplet velocities at different positions between the electrodes are calculated through image analyses using ImageJ®. Each calculated velocity represents the average value over five independent tri-
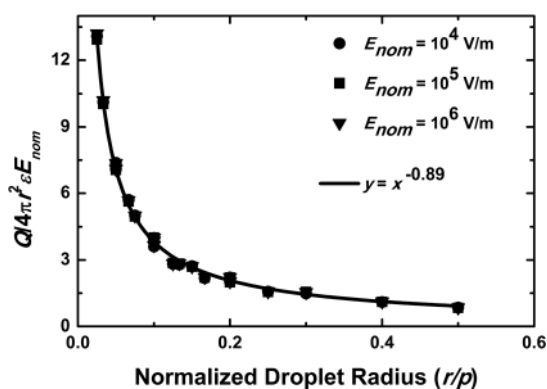

Fig. 4 The normalized equilibrium droplet charge is approximately inversely proportional to the normalized droplet radius r under combinations of geometric parameters examined in the present study.

als ($N = 5$) performed under the nominally identical bias voltage and geometric parameters. The estimated errors e, indicated by the error bars in this and subsequent figures, account for both the random error (S_N) as estimated from the standard deviations at the 95% confidence level and the uncertainty in the measured droplet positions due to finite spatial resolution of our imaging system:

$$e = \sqrt{S_N^2 + u^2} \qquad (9)$$

We compare the measured droplet velocities with the so-called droplet terminal velocities, which are obtained by equating the predicted electrophoretic force at each droplet location to the steady-state drag force. The steady-state drag force F_x of a droplet moving parallel to a horizontal surface at a constant velocity U can be determined from ref. 28 and 29:

$$F_x = 6\pi\mu rUf \qquad (10)$$

$$f = \left(\frac{8}{15} + \frac{64}{375}\epsilon\right)\log\left(\frac{2}{\epsilon}\right) + 0.5846 \qquad (11)$$

where μ is the viscosity of the surrounding dielectric fluid after correcting for the finite viscosity of the liquid droplet, r is the radius of the droplet and ϵ is the ratio of the gap h (Fig. 2) to the droplet radius r.

In Fig. 5(A), the filled symbols represent the measured instantaneous velocities of droplets under three actuation voltages: 150 V, 200 V, and 250 V. These voltage values are chosen to be comparable to the outputs from our piezoelectric elements. The droplet radius is 0.63 mm, and the electrode pitch is 1.76 mm. The lines correspond to the predicted droplet terminal velocities at different positions between the electrodes.

The predicted terminal velocities agree reasonably well with the experimentally measured velocities in the middle sections ($0.3 < d_x/p < 0.7$) for actuation voltages of 150 V and 200 V. They deviate from the experimental data near the starting and terminal electrodes. This is due mainly to the fact that our steady-state model ignores the finite inertia of the droplets and the dynamic variations in droplet charges due to finite leakage. The model overpredicts the velocities at the highest actuation voltage (250 V) due to incomplete initial droplet charging as further discussed later in the section. The droplet translational velocity decreases quite substantially with decreasing bias voltages due to the combined effect of smaller droplet charges and smaller electric fields. For all the cases shown in Fig. 5(A), the droplet velocity increases with d_x/p. That is, a larger electrophoretic force acts on the droplet as it approaches the terminal electrode of the opposite polarity than as it departs from the charging electrode of the same polarity.
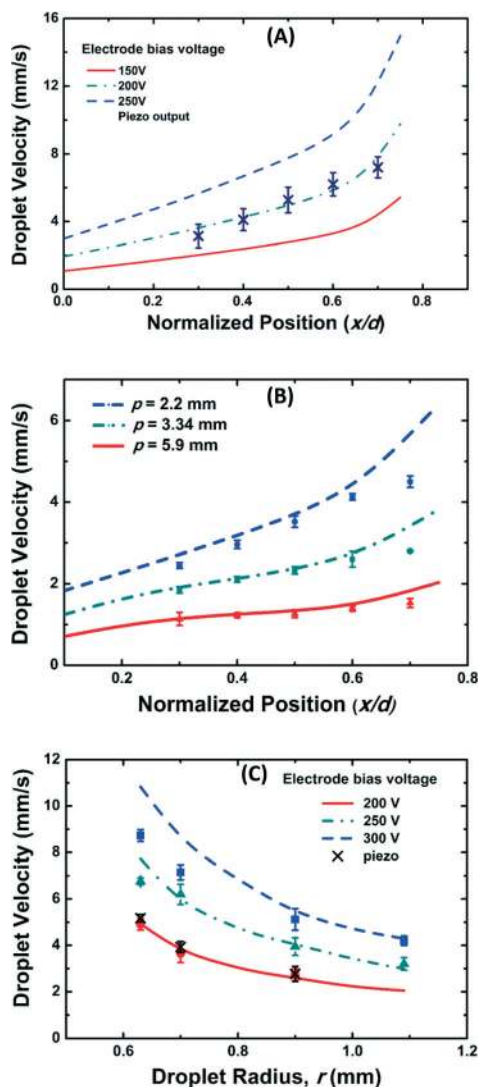
Fig. 5 (A) Measured (symbols) and predicted (lines) droplet velocities as a function of the normalized distance from the charging electrode under different applied voltages. The electrode pitch p = 1.76 mm and the droplet radius r = 0.63 mm. (B) Variations in the local droplet translational velocity for different values of the electrode pitch. The actuation voltage is fixed at 200 V, and the droplet radius is fixed at 0.7 mm. (C) Variations in the droplet velocity at the middle point between the electrodes (x/p = 0.5) for four different droplet radii and three different actuation voltages. The r/p ratio is kept constant at 0.33 for all the cases.

Aqueous droplets are also successfully actuated when the electrodes are biased using the piezoelectric elements. The measured droplet translational velocities, marked with crosses in Fig. 5(A), are similar to those obtained at 200 V using an external power supply.

The total droplet transit time across the two electrodes was <1 s for all the cases studied here. The voltage applied by piezoelectric elements may be assumed to remain constant only when this total droplet transit time is much less than the discharging time of the piezoelectric elements. Charge dissipation through a dielectric liquid is typically modelled as:

$$Q(t) = Q_0 \mathrm{e}^{-\frac{t}{\tau_r}} \qquad (12)$$

Here, τ_r is the relaxation time constant and is equal to the ratio of the material permittivity to the conductivity.

This consideration leads to a second criterion for reliable transport of droplets using our piezoelectric actuation scheme: the droplet transit time (between electrode pairs) must be sufficiently short when compared with both the discharging time of piezoelectric elements and the charge relaxation time of the dielectric medium.

In our piezoelectric elements, the RC time constant is estimated to be 30 seconds from their measured electrical capacitance and resistance. The estimated value of τ_r for the silicone oil used in the present study is >200 s, much larger than the RC time constant of the piezoelectric elements.

We next repeat the experiments for different values of the electrode pitch. In Fig. 5(B), the solid lines show the predicted terminal velocities of droplets with a radius of 0.7 mm at an electrode bias voltage of 200 V. The electrode pitch p is varied from 2.2 to 5.9 mm. The predicted droplet terminal velocity decreases rapidly with increasing pitches. The droplets are also successfully actuated with the piezoelectric elements for electrode pitches of 2.2 and 3.34 mm. The measured translational velocities are plotted as filled symbols in Fig. 5(B). For the largest pitch (5.9 mm), the droplet transit time approaches the discharge time of the piezoelectric elements and a stable actuation voltage cannot be maintained. To help further discuss our results, we instead used an external power supply to obtain the droplet velocities for the case with the largest electrode pitch.

Fig. 5(B) also shows that spatial variations in the local droplet velocity along d_x qualitatively differ for different electrode pitches. For a large electrode pitch of 5.9 mm, the local droplet velocity stays relatively constant for $0.3 < d_x/p < 0.7$. In contrast, for the smaller pitches, the local droplet velocity increases monolithically with d_x/p as the droplet continues to spatially "sample" highly non-uniform electric fields near the electrodes.

Note that the above results are obtained by varying the electrode pitch for a fixed droplet radius. We may, alternatively, consider cases where the droplet radius is varied at the same time such that the droplet radius to the electrode pitch ratio (r/p) stays constant. In this case, spatial variations in the local droplet velocity along x remain qualitatively similar for different electrode pitches considered in the present study. Representative simulation results for r/p = 0.1 are presented in Appendix B.

We next determine droplet velocities at the mid-point between the two electrodes as a function of the droplet radius while keeping r/p constant (approximately 0.33). The experiments were repeated for three different bias voltages: 200 V, 250 V and 300 V. The filled symbols in Fig. 5(C) are the measured values, which agree reasonably well with the predicted terminal velocities (lines). With r/p being kept constant, the droplet velocity decreases with increasing droplet sizes as the

nominal electric field and the charge density at the droplet surface decrease. For the largest droplet of radius 1.1 mm, the piezoelectric actuation is insufficient due in part to a large transit time and in part to large droplet inertia.

At high actuation voltages (250 V and 300 V in Fig. 5(C)), one notes that the measured velocities are lower than the predicted values for the smaller droplet sizes (and electrode pitches). Similar overprediction is also noted in Fig. 5(A) at an actuation voltage of 250 V. One possible origin of these discrepancies is a partial or incomplete charging of droplets under high electric fields present in these situations. That is, the actual amount of droplet charges is less than Q_{eq}, which in turn leads to reduced electrophoretic force.

For a droplet with finite conductivity, a finite charging time is necessary for the droplet to reach equipotential with the charging electrode. If the droplet leaves the electrodes within this charging period, then the droplet will acquire only a fraction of Q_{eq}.

The charging time is a function of the conductivity of the droplet, the dielectric properties of the fluids, and the contact area between the droplet and the charging electrode. We use transient numerical simulations to estimate the charging time to be of the order of a few to a few tens of milliseconds for aqueous droplets of the sizes and electrical properties used in the present study (see Appendix A). This is comparable to or larger than previously estimated contact times at local electric fields of approximately 3 kV cm^{-1}.[21,30] We therefore expect that the droplet is only partially charged before it is detached from the charging electrode under high bias voltages. This in turn leads to decreased electrophoretic forces and hence smaller droplet translation velocities.

Droplet transport and merging

Fig. 6 shows time-sequence optical images of a single water droplet with a volume of approximately 2 μL that is being transported between adjacent electrodes through a sequence of finger-powered ECD actuations. The electrode pitch p is 2.08 mm, and the droplet radius r is ~0.78 mm. To transport
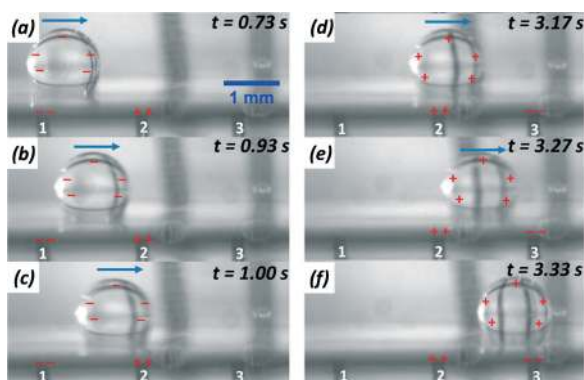
a droplet in a desired direction, one needs to sequentially alternate the relative polarities of the electrode pairs. For example, referring to Fig. 6(c) to (d), the polarities of Electrodes 1 and 3 are interchanged when the droplet reaches the nearest approaching electrode (Electrode 2). This allows the positively charged droplet on Electrode 2 to continue moving to Electrode 3.

Fig. 7(A) shows the merging of two DI water droplets using the same electrode configuration as above. The two droplets are oppositely charged in advance. The transparent droplet on the left is positively charged on Electrode 2, whereas the dyed droplet on the right is negatively charged on Electrode 3. When actuated to approach each other, the two droplets merge almost instantaneously upon contact through electrostatic interaction.

Enhanced mixing can be achieved by continuously transporting the droplet back and forth between two electrodes and thereby inducing internal flows. This can be achieved readily in EPD microfluidic devices by simply maintaining the electrode bias, that is, by keeping the piezoelectric elements bent. The oscillatory motion results because the polarity of the droplet keeps reversing as the droplet alternately contacts one of the two electrodes. Enhanced mixing is demonstrated by mixing a dyed droplet with a clear droplet (Fig. 7(B)) with or without the sustained electrode bias (EPD enhanced *vs.* static). One may achieve further reduction in the mixing time by breaking the symmetry and stirring more chaotic flows[31] inside the droplet using a 2D array of electrodes rather than a linear array.
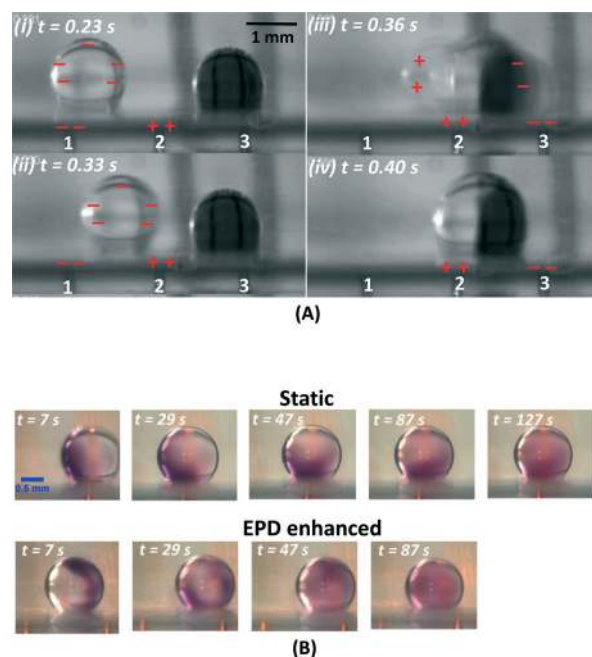

(A)

(B)

Fig. 7 (A) A time sequence showing the merging of two oppositely charged droplets. (B) Mixing by pure diffusion (top) compared with enhanced mixing using EPD actuation (bottom). The radius of the merged droplet is approximately 0.75 mm.

Fig. 6 A time sequence from (a) to (f) showing continuous droplet transport by finger-powered EPD. The droplet volume is approximately 2 μL, and the electrode pitch is 2.08 mm. The r/p ratio is ~0.37.

One important challenge in the biomedical applications of microfluidic devices originates from high viscosities, extreme pH values or other unusual properties of samples, such as body fluids. We show in Fig. 8 successful transport of droplets of human body fluids (saliva and urine) and an alkaline solution across three electrodes. The pH values for these droplets vary from 5.8 (human urine) to 9 (sodium hydroxide solution).

Mechanical system for programmed operations

Relying on just human fingers to precisely deflect multiple piezoelectric elements in a complex sequence is not realistic for practical implementation of our concept. To convert finger (or hand) motions into a sequence of controlled and reproducible deflections of piezoelectric elements, we propose a finger/hand-rotated drum system. Our design, shown in Fig. 9, consists of a drum and an array of mechanical levers. This design is analogous to that of a music box where pins (or embossed protrusions) formed on a cylinder are used to pluck an array of cantilever beams in a specific sequence. On the surface of our drum is a set of protrusions in pre-programmed locations. The drum surface is patterned like a toothed gear so that reusable plastic protrusions can be placed on desired locations. The mechanical levers are mounted in a see-saw configuration using a common shaft on a fixed fulcrum. One end of each lever is linked mechanically to piezoelectric elements. As the drum is manually rotated, the protrusions push down on the mechanical levers, which in turn deflect corresponding piezoelectric elements.

We experimentally examine the consistency of voltage pulses generated using the mechanical drum system. Each piezoelectric element unit consists of two piezoelectric elements connected electrically in series and mechanically to the same lever. The drum is rotated at approximately 100 degrees per second, resulting in voltage pulses with a duration of approximately 0.1 s. This duration is comparable to typical droplet transit times across two adjacent electrodes.

Fig. 9 A finger/hand-rotated drum system consisting of a drum with protrusions and an array of mechanical levers mounted in a see-saw configuration. One end of each lever is linked mechanically to a piezoelectric element. In this particular device, the outer diameter of the drum is approximately 6 cm; the width and height of each protrusion are 3 mm; the length of the levers is approximately 10 cm, and the lever ratio is approximately 1:7.

Fig. 10 shows the voltage pulses measured during repetitive deflections of one of the piezoelectric units. Table 2 summarizes the results obtained from three independent piezoelectric element units. The results show that our drum system provides fairly consistent voltage pulses (standard deviations of approximately 4%) with smaller amplitude variations than human fingers.
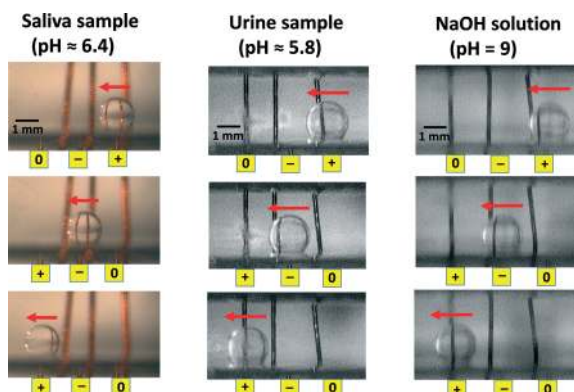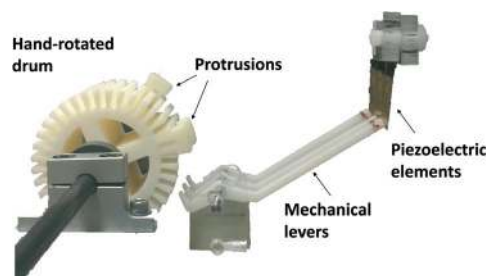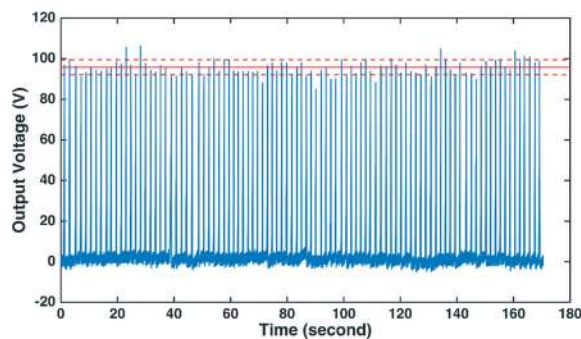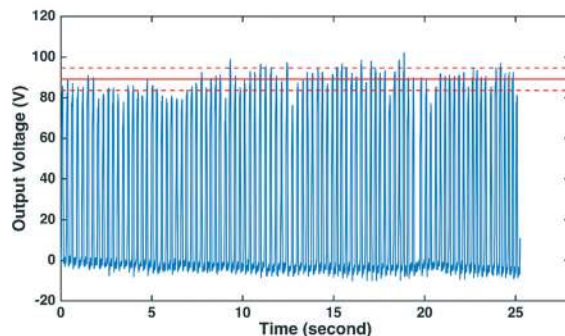

Fig. 8 Sequential images (top to bottom) of a saliva droplet, a urine droplet and a NaOH droplet transported via finger-powered EPD. The droplet radius is ~0.7 mm, and the droplet radius to electrode pitch ratio (r/p) is approximately 0.4.

Fig. 10 Voltage outputs from a single piezoelectric element unit over multiple deflections (A) by the mechanical drum system and (B) by a human finger. The solid red lines indicate the average voltage outputs, and the dotted red lines represent one standard deviation.

Table 2 Measured voltage pulse outputs from 3 independent piezoelectric element units over 100 deflections either by the drum system or by human fingers

Unit	Voltage (V) by drum	Voltage (V) by finger
1	90.2 ± 3.4	87.4 ± 7.9
2	97.2 ± 1.6	99.8 ± 7.3
3	93.8 ± 2.6	90.5 ± 6.3

Base electrode matrix and electric connection schemes

The number of piezoelectric elements one can use in practical portable EPD devices is limited. We explore a base electrode matrix and its connection scheme to realize different microfluidic functions using a minimum number of piezoelectric elements. Similar schemes[32] were explored for EWOD digital microfluidic devices. The electric polarities of the electrodes, however, were not fixed in those studies as they implicitly assumed the availability of external power supplies/switching circuits. In contrast, in our finger-powered EPD microfluidic device, the polarity of each piezoelectric element unit is pre-fixed to facilitate their mechanical integration.

For a square electrode matrix with a size of $n \times n$ ($n > 3$), the minimum number of piezoelectric element units necessary to actuate a droplet located at any given position in any of the four independent directions (up, right, down or left)

(A)

(B)

(C)   **(D)**
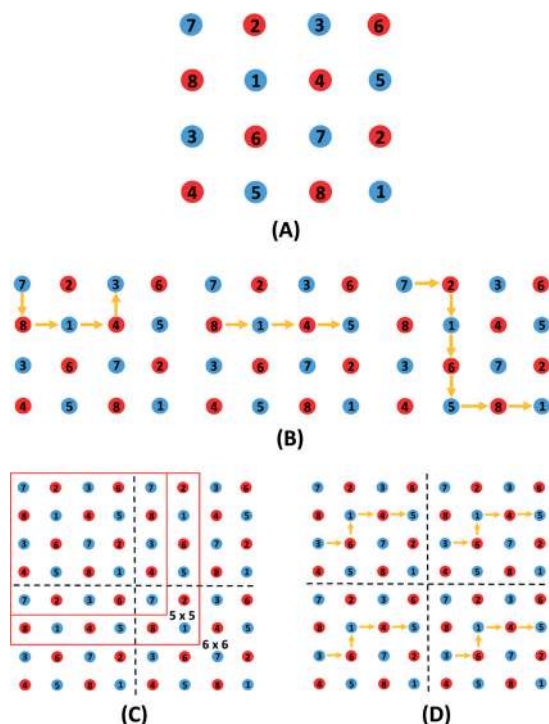
Fig. 11 (A) Base electrode matrix of size 4 × 4. (B) Sample droplet actuation paths one can realize using the 4 × 4 base electrode matrix. (C) By replicating the base electrode matrix, one can power a larger electrode matrix using 8 piezoelectric element units. (D) Parallel execution of a set of identical operations on 4 droplets.

is 8 (see Appendix C). Fig. 11(A) shows one design of a base electrode matrix of size 4 × 4. We use the even numbers (red) to label the electrodes connected to the four piezoelectric elements of the positive polarity and the odd numbers (blue) to label the electrodes connected to the remaining four piezoelectric elements of the negative polarity. Fig. 11(B) shows sample droplet transport paths that can be achieved using the base electrode matrix. Other possible path designs for operations such as droplet merging and storage are provided in the ESI.† One can replicate this basic matrix multiple times (Fig. 11(C)). A minimum of 8 piezoelectric elements may then be used to actuate a droplet across a larger electrode matrix or to perform an identical set of actuations for multiple droplets in parallel (Fig. 11(D)).

Electrically connecting multiple electrodes to a single piezoelectric element unit allows significant reduction in the number of piezoelectric elements and hence the size and cost of the overall system. Interference among these electrodes, however, may present a potential issue.

We experimentally test our 4 × 4 base electrode matrix connected to 8 independent piezoelectric element units. The units are deflected in pre-programmed sequences using our mechanical drum system. We successfully demonstrate sequential droplet actuations over multiple paths covering different electrode sites on the matrix. The snapshot images are shown in Fig. 12(A) for droplet linear transport and in Fig. 12(B) for merging of two droplets and subsequent enhanced mixing. The corresponding videos are provided in the ESI.†

To help quantify the interfering influence of adjacent electrodes, we conduct additional numerical simulations. The simulations show that the magnitude of interfering forces is less than 10% of the main driving force under typical actuation conditions used in the present study. Further details are provided in the ESI.†

Conclusions

We demonstrate finger-powered electrophoretic transport of droplets (EPD) for digital microfluidics. The mechanical energy provided by human fingers can be converted using an array of piezoelectric elements into sufficient electrical energy to charge and electrophoretically actuate droplets.

Numerical models for droplet electrical charging and resulting electrophoretic forces are developed and experimentally validated to help establish the design criteria for finger-powered EPD actuation. The capacitance of the piezoelectric elements needs to be much larger than the droplet/electrode system, and the droplet transit time (across two electrodes) needs to be sufficiently smaller than the discharge time of the piezoelectric elements. The latter in turn limits the electrode pitch.

We successfully demonstrate linear transport and merging of aqueous droplets using finger-powered EPD. Transport of
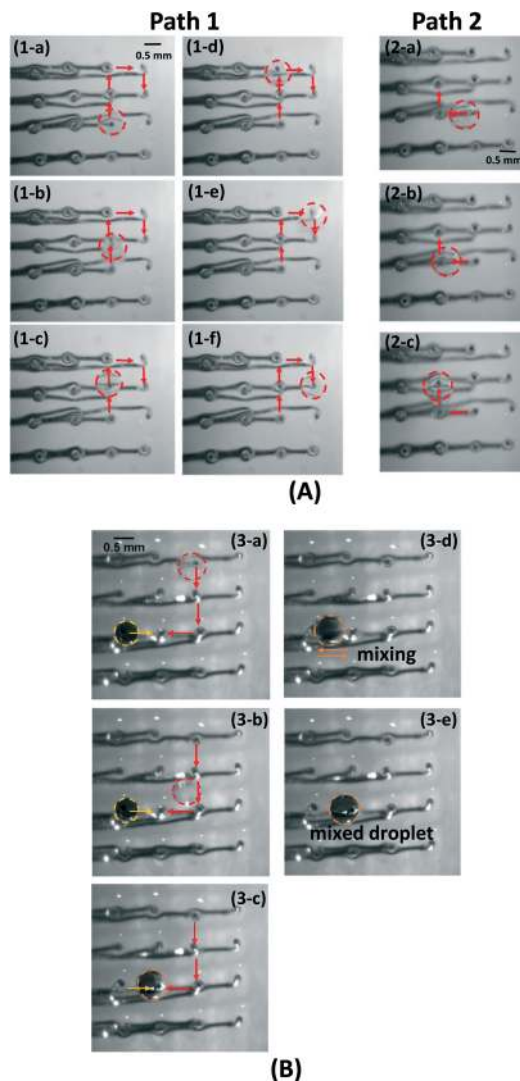
Fig. 12 (A) Demonstration of droplet actuation along different paths on the 4 × 4 base electrode matrix, which is connected to 8 piezoelectric element units. (B) Demonstration of the merging and subsequent enhanced mixing of two droplets on the base electrode matrix.

human body fluids, such as saliva and urine droplets, is also demonstrated.

To facilitate practical implementation of portable microfluidic devices based on our approach, we design a finger/hand-rotated drum system to reliably control deflections of multiple piezoelectric elements in a pre-programmed manner. We also report a base electrode matrix and electric connection schemes to implement different microfluidic functions while using a minimum number of piezoelectric elements. We successfully demonstrate multiple programmed droplet actuations using our integrated system with a 4 × 4 base electrode matrix and a mechanical drum with protrusions. Our work establishes an engineering foundation for systematic design and implementation of finger-powered EPD devices for portable microfluidic applications.

Appendix A

In the main text, we assumed that the droplet acquires maximum equilibrium charges before it is detached from the charging electrode. To examine the validity of this assumption, we directly simulate a transient charging process for an aqueous droplet.

The model is shown schematically in Fig. 13. A spherical droplet of radius R, conductivity σ, and permittivity ε_i is in contact with one of the electrodes through contact area A. The droplet and electrodes are immersed in dielectric oil. Subscripts "i", "o" and "s" are used to label the variables associated with the region inside the droplet, in the surrounding oil and at the droplet interface, respectively. We assume electrical charges are transported by ohmic volume conduction within the droplet. We also assume that all the dielectric properties are constant.

We solve the following transient continuity equation:

$$\frac{\partial \rho_s^{(t+1)}}{\partial t} + \nabla \cdot \vec{J}^{(t)} = 0 \tag{A-1}$$

The current density is related to the electric field within the droplet:

$$\vec{J}^{(t)} = \sigma \vec{E}^{(t)} = -\sigma \nabla V^{(t)} \tag{A-2}$$

At each time t, the electric field $E^{(t)} = -\nabla V^{(t)}$ is obtained by solving the Laplace equation:
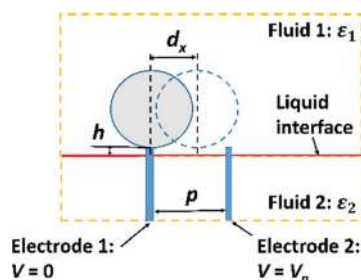
$$\nabla^2 V^{(t)} = 0 \tag{A-3}$$

The boundary conditions are given as follows:
• Constant electric potentials at the two electrode surfaces:

$$V = 0 \quad \text{on Electrode 1} \tag{A-4}$$

$$V = V_n \quad \text{on Electrode 2} \tag{A-5}$$

• Continuity of the electrostatic displacement vector across the droplet surface, where ρ_s is the surface charge density:

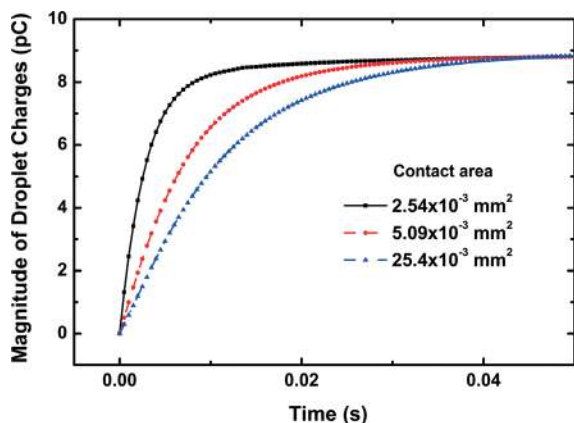Fig. 13 Schematic illustration of the model used for the simulation of transient droplet charging.

Fig. 14 Predicted temporal evolution of the droplet charges for three different droplet–electrode contact areas.
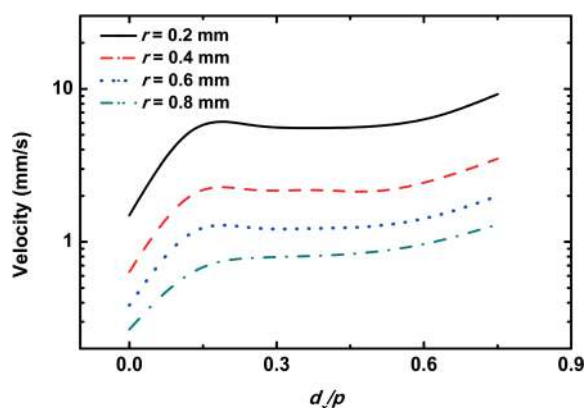

Fig. 15 Predicted terminal velocities of electrophoretically actuated droplets with a fixed value of $r/p = 0.1$ for different combinations of r and p.

$$\varepsilon_o \frac{\partial V_o^{(t)}}{\partial n} - \varepsilon_i \frac{\partial V_i^{(t)}}{\partial n} = \rho_s^{(t)} \qquad \text{(A-6)}$$

• Symmetry boundary conditions on the outer boundaries:

$$\varepsilon_o \frac{\partial V}{\partial n} = 0 \qquad \text{(A-7)}$$

The total charge at any given time t is obtained by integrating the surface charge density on the droplet surface S_d. The predicted temporal evolution of the amount of charges on the droplet is shown in Fig. 14. The droplet radius is 0.63 mm, the electrode pitch is 1.76 mm and the applied voltage is 100 V. The results are presented for three different contact areas (A), *i.e.* 2.5×10^{-2} mm^2, 5×10^{-3} mm^2 and 2.5×10^{-3} mm^2. The largest value is equal to the area of the electrode top surface in our study and the others to 1/5 and 1/10 of that value. The droplet charges approach the maximum (in magnitude) equilibrium value at different rates depending the contact area. The estimated charging times range from a few

tens of milliseconds, increasing with decreasing contact areas.

Appendix B

Fig. 15 shows the predicted terminal velocities (in log scale) for a fixed r/p ratio of 0.1 under a bias voltage of 200 V. The droplet radius is varied from 0.2 to 0.8 mm and the electrode pitch from 2 to 8 mm. Note that spatial variations in the local droplet velocity with increasing traveling distance (d_x/p) are qualitatively similar for all the cases simulated.

Appendix C

For a square electrode matrix of size $n \times n$ (with $n > 3$), we first show that the minimum number of piezoelectric elements necessary to actuate a droplet at any given position in any of the four independent directions (up, right, down or left) is 8.

We use (i, j) to indicate the row and column of each electrode, $c(i, j) \subset \{+, -\}$ to indicate its polarity and $p(i, j)$ to indicate the piezoelectric element connected to that electrode.

1. Consider electrode (i, j), where $i \neq 0$, $j \neq 0$, $i \neq n$, and $j \neq n$. This center electrode is surrounded by four adjacent electrodes: $(i - 1, j)$, $(i, j + 1)$, $(i + 1, j)$ and $(i, j - 1)$, corresponding to each of the four directions of possible linear droplet actuation. We use Ω to represent the set of piezoelectric elements connected to these 4 surrounding electrodes

$$\Omega = \{p(i - 1, j), p(i, j + 1), p(i + 1, j), p(i, j - 1)\}$$

2. For EPD actuation of a droplet initially located at (i, j), the destination electrode must have the opposite polarity. That is, we must have $c(i - 1, j) = c(i, j + 1) = c(i + 1, j) = c(i, j - 1) = -c(i, j)$. In other words, the four electrodes centered around one common electrode must have the same polarity, opposite to that of the center electrode.

3. A dummy electrode with no electric connection to a piezoelectric element is not allowed in the matrix.

4. We first prove that $\min(|\Omega|) = 4$. Let's assume that, for a particular center electrode m, $|\Omega_m| < 4$. At least 2 of the adjacent electrodes would then be connected to the same piezoelectric elements. Interference would occur when a droplet initially located on the center electrode m is to be actuated to one of these adjacent electrodes. Therefore, we must ensure that $|\Omega| \geq 4$ for any center electrode.

5. For a matrix of any size greater than 3×3, there are at least two adjacent center electrodes, denoted as A and B. We already showed in steps 2 and 4 that $|\Omega_A| \geq 4$ and $|\Omega_B| \geq 4$ and that the piezoelectric elements in each set must each have the same polarity. Since the polarities of electrodes A and B themselves must be opposite (one is an adjacent electrode for the other), so do the piezoelectric elements in the two sets. That is, $\Omega_A \cap \Omega_B = \emptyset$. Therefore, $|\Omega_A \cup \Omega_B| = 8$.

References

1   R. Gerbers, W. Foellscher, H. Chen, C. Anagnostopoulos and M. Faghri, *Lab Chip*, 2014, **14**, 4042–4049.

2   J. Hu, S. Wang, L. Wang, F. Li, B. Pingguan-Murphy, T. J. Lu and F. Xu, *Biosens. Bioelectron.*, 2014, **54**, 585–597.

3   D. M. Cate, J. A. Adkins, J. Mettakoonpitak and C. S. Henry, *Anal. Chem.*, 2015, **87**, 19–41.

4   G. A. Posthuma-Trumpie, J. Korf and A. Amerongen, *Anal. Bioanal. Chem.*, 2009, **393**, 569–582.

5   X. Li, P. Zwanenburg and X. Liu, *Lab Chip*, 2013, **13**, 2609–2614.

6   H. Chen, J. Cogswell, C. Anagnostopoulos and M. Faghri, *Lab Chip*, 2012, **12**, 2909–2913.

7   R. Fobel, A. E. Kirby, A. H. C. Ng, R. R. Farnood and A. R. Wheeler, *Adv. Mater.*, 2014, **26**, 2838–2843.

8   R. R. Niedl and C. Beta, *Lab Chip*, 2015, **15**, 2452–2459.

9   E. Elizalde, R. Urteaga and C. L. A. Berli, *Lab Chip*, 2015, **15**, 2173–2180.

10 I. K. Dimov, L. Basabe-Desmonts, J. L. Garcia-Cordero, B. M. Ross, A. J. Ricco and L. P. Lee, *Lab Chip*, 2011, **11**, 845–850.

11 K. J. Cha and D. S. Kim, *Biomed. Microdevices*, 2011, **13**, 877–883.

12 D. Juncker, H. Schmid, U. Drechsler, H. Wolf, M. Wolf, B. Michel, N. de Rooij and E. Delamarche, *Anal. Chem.*, 2002, **74**, 6139–6144.

13 T. Kokalj, Y. Park, M. Vencelj, M. Jenko and L. P. Lee, *Lab Chip*, 2014, **14**, 4329–4333.

14 K. Iwai, K. C. Shih, X. Lin, T. A. Brubaker, R. D. Sochol and L. Lin, *Lab Chip*, 2014, **14**, 3790–3799.

15 G. Korir and M. Prakash, *PLoS One*, 2015, **10**(3), e0115993, DOI: 10.1371/journal.pone.0115993.

16 X. Xu, L. Sun, L. Chen, Z. Zhou, J. Xiao and Y. Zhang, *Biomicrofluidics*, 2014, **8**, 064107.

17 C. Peng, Z. Zhang, C.-J. Kim and Y. S. Ju, *Lab Chip*, 2014, **14**, 1117–1122.

18 D. J. Im, M. M. Ahn, B. S. Yoo, D. Moon, D. W. Lee and I. S. Kang, *Langmuir*, 2012, **28**, 11656–11661.

19 D. J. Im, J. Noh, D. Moon and I. S. Kang, *Anal. Chem.*, 2011, **83**, 5168–5174.

20 V. Miralles, A. Huerre, H. Williams, B. Fournié and M.-C. Jullien, *Lab Chip*, 2015, **15**, 2133–2139.

21 M. Hase, S. N. Watanabe and K. Yoshikawa, *Phys. Rev. E: Stat., Nonlinear, Soft Matter Phys.*, 2006, **74**, 046301.

22 S. Mhatre and R. M. Thaokar, *Phys. Fluids*, 2013, **25**, 072105.

23 C.-P. Lee, H.-C. Chang and Z.-H. Wei, *Appl. Phys. Lett.*, 2012, **101**, 014103.

24 A. M. Drews, M. Kowalik and K. J. M. Bishop, *J. Appl. Phys.*, 2014, **116**, 074903.

25 D. J. Im, B. S. Yoo, M. M. Ahn, D. Moon and I. S. Kang, *Anal. Chem.*, 2013, **85**, 4038–4044.

26 M. W. Hooker, Properties of PZT-Based Piezoelectric Ceramics Between −150 and 250 °C, Hampton, NASA/CR-1998-208708, 1998, Retrieved from http://ntrs.nasa.gov/search.jsp?R=19980236888.

27 *Measurement Specialties Inc, Piezo Film Sensors Technical Manual*, Available online: http://www.meas-spec.com/downloads/Piezo_Technical_Manual.pdf.

28 A. J. Goldman, R. G. Cox and H. Brenner, *Chem. Eng. Sci.*, 1967, **22**, 653–660.

29 M. E. O'Neill and K. Stewartson, *J. Fluid Mech.*, 1967, **27**, 705–724.

30 Y.-M. Jung, H.-C. Oh and I. S. Kang, *J. Colloid Interface Sci.*, 2008, **322**, 617–623.

31 T. Ward and G. M. Homsy, *J. Fluid Mech.*, 2006, **547**, 215–230.

32 T. Xu, K. Chakrabarty and V. K. Pamula, in *Proc. IEEE/ACM Int. Conf. on Computer-Aided Design*, 2008, pp. 297–301.